AGU PUBLICATIONS

JGR

Journal of Geophysical Research: Space Physics

RESEARCH ARTICLE
10.1002/2017JA024424

Key Points:
- Varying tetrahedron sizes are used to study magnetic curvature and vorticity analyses in a MHD simulation of KH waves at the magnetopause
- In the trailing edge of the KH wave, the magnetic curvature across the magnetopause points in opposite directions
- The development of negative vorticity on the dusk magnetospheric side is contrary to expected and persists in the saturation phase

Supporting Information:
- Supporting Information S1
- Movie S1
- Movie S2

Correspondence to:
R. Kieokaew,
rk359@exeter.ac.uk

Citation:
Kieokaew, R., Foullon, C., & Lavraud, B. (2018). Four-spacecraft magnetic curvature and vorticity analyses on Kelvin-Helmholtz waves in MHD simulations. *Journal of Geophysical Research: Space Physics*, *123*. https://doi.org/10.1002/2017JA024424

Received 1 JUN 2017
Accepted 24 DEC 2017
Accepted article online 3 JAN 2018

Four-Spacecraft Magnetic Curvature and Vorticity Analyses on Kelvin-Helmholtz Waves in MHD Simulations

Rungployphan Kieokaew[1], Claire Foullon[1], and Benoit Lavraud[2]

[1]CGAFD, Mathematics, CEMPS, University of Exeter, Exeter, UK, [2]Institut de Recherche en Astrophysique et Planétologie, Université de Toulouse, Toulouse, France

Abstract Four-spacecraft missions are probing the Earth's magnetospheric environment with high potential for revealing spatial and temporal scales of a variety of in situ phenomena. The techniques allowed by these four spacecraft include the calculation of vorticity and the magnetic curvature analysis (MCA), both of which have been used in the study of various plasma structures. Motivated by curved magnetic field and vortical structures induced by Kelvin- Helmholtz (KH) waves, we investigate the robustness of the MCA and vorticity techniques when increasing (regular) tetrahedron sizes, to interpret real data. Here for the first time, we test both techniques on a 2.5-D MHD simulation of KH waves at the magnetopause. We investigate, in particular, the curvature and flow vorticity across KH vortices and produce time series for static spacecraft in the boundary layers. The combined results of magnetic curvature and vorticity further help us to understand the development of KH waves. In particular, first, in the trailing edge, the magnetic curvature across the magnetopause points in opposite directions, in the wave propagation direction on the magnetosheath side and against it on the magnetospheric side. Second, the existence of a "turnover layer" in the magnetospheric side, defined by negative vorticity for the duskside magnetopause, which persists in the saturation phase, is reminiscent of roll-up history. We found significant variations in the MCA measures depending on the size of the tetrahedron. This study lends support for cross-scale observations to better understand the nature of curvature and its role in plasma phenomena.

1. Introduction

Four-spacecraft missions provide a unique opportunity to study plasma phenomena in the Earth's magnetospheric environments with high potential for resolving spatiotemporal fluctuations. The Earth's magnetosphere outer boundary, the magnetopause, is the site of plasma processes that allow the entry of solar wind plasma to the magnetosphere. Depending on the interplanetary magnetic field (IMF) configuration, mechanisms that can operate at this boundary are different. Kelvin-Helmholtz (KH) instabilities, arising from a shear flow at the interface, are believed to be common under northward IMF conditions. Numerous observations have been studied by the four-spacecraft *Cluster* (Escoubet et al., 2001) and recently the Magnetospheric Multiscale (MMS) missions (Burch et al., 2015). KH instabilities have been proposed as a candidate mechanism for the penetration of solar wind plasma, the widening of the low-latitude boundary layer, and the triggering of ultralow-frequency waves. Solar wind plasma entry is possible via magnetic reconnection (e.g., Nykyri & Otto, 2001) and turbulence (e.g., Matsumoto & Hoshino, 2004) inside rolled-up KH vortices. Analyses of KH events at the magnetopause help us to understand the evolution and mechanisms associated with the waves.

There are two approaches to study KH waves at the magnetopause. Particle distributions are commonly used to reveal particle mixing inside KH vortices (e.g., Nishino et al., 2007; Taylor & Lavraud, 2008). Lower-density and faster-than-sheath (LDFTS) plasma is a distinct signature associated with rolled-up KH vortices (Takagi et al., 2006). However, other contributing factors such as the presence of a plasma depletion layer can mimic the features of the LDFTS plasma (Plaschke et al., 2014). Investigations of surface boundary geometry, on the other hand, are less common. Periodic surface wave analysis can be used to sketch the spatial structures straightforwardly from time series of KH waves (De Keyser & Roth, 2003). Grad-Shafranov-like reconstruction developed by Sonnerup et al. (2006) is used to reconstruct streamlines surrounding the spacecraft path of a plasma flow transverse to the magnetic field structure of KH waves (e.g., Hasegawa et al., 2007).

Multispacecraft timing analysis (Russell et al., 1983) has been used to determine the magnetopause boundary inclinations during surface wave passages in the four-spacecraft Cluster (Owen et al., 2004; Foullon et al., 2008) and MMS data (Plaschke et al., 2016). A steeper leading edge than the trailing edge is expected for KH waves. The method requires planarity of the boundary within the spacecraft separation, which may not always be satisfied for the surface wrapping around KH vortices.

Magnetic curvature is intrinsic to curved magnetic fields where the magnetic energy is stored in the form of magnetic tension. In situ magnetic curvature has been resolved by the four-spacecraft technique called "magnetic curvature analysis" (MCA) (Shen et al., 2003). The method applies magnetic field gradient tensors that can be found either through the least squares minimization (Harvey, 1998) or the barycentric method (Chanteur, 1998). To extend the idea of the surface wave analysis to three-dimensional, nonplanar structures such as KH waves, we aim to explore the applicability of MCA. The method yields magnetic curvature, which, by definition, points in the direction of the magnetic tension force. The reciprocal of the curvature the so-called "curvature radius" can be used to estimate the scale size of the magnetic structure. The method has been applied to Cluster observations of current sheets (e.g., Runov et al., 2006; Shen et al., 2008), plasmoids (e.g., Zhang et al., 2013), ring current (e.g., Shen et al., 2014), and magnetic flux ropes (e.g., Yang et al., 2014). Particle pitch angle scattering is inferred from magnetic curvature in magnetic reconnection sites in the ion diffusion regions (e.g., Zhang et al., 2016) and in the electron diffusion regions (e.g., Cao et al., 2017; Lavraud et al., 2016).

Magnetic fields threading through KH waves may involve complex three-dimensional configurations. Three-dimensional kinetic simulations show that compressed current sheets along the KH wave trailing edges can give rise to magnetic flux ropes over a range of oblique angles (Nakamura et al., 2013). These flux ropes propagate with the shear flow and later merge with parent vortices. Some observations suggest midlatitude reconnection of three-dimensional field lines interweaving through KH waves at the equatorial plane (Bavassano Cattaneo et al., 2010). Statistical studies on MMS observations by Vernisse et al. (2016) show that this process can allow plasma entry even though the KH instability remains in its linear stage. Three-dimensional simulations show that magnetic field lines connecting between the Southern and Northern Hemispheres can be twisted by the vortical flows at the equatorial plane, creating a favorable condition for reconnection at midlatitudes (Faganello et al., 2012; Leroy & Keppens, 2017). Resolving magnetic curvature of KH waves may help in understanding distortion of Earth's magnetic field lines between low and high latitudes and, consequently, how they may reconnect with the magnetosheath magnetic field.

Vorticity is intrinsic to any flow system that exhibits swirling patterns such as vortical flows in KH vortices. Despite that, in situ vortical flow studies in magnetospheric environments are limited. Four spacecraft make it possible to resolve vorticity $\mathbf{\Omega} = \nabla \times \mathbf{V}$, where $\mathbf{V}$ is the velocity field, using either the least squares method (Harvey, 1998) or the barycentric estimator (Chanteur, 1998). Vorticity in observed KH events has been resolved in three-spacecraft measurements by Time History of Events and Macroscale Interactions during Substorms (THEMIS) and Cluster by Shen et al. (2012). This work further suggests that pulsed-enhanced periodic vorticity can be the signature of rolled-up KH waves. Using global MHD simulations, Collado-Vega et al. (2013) studied plasma vortices (quantified with a velocity gradient tensor) under various IMF clock angles and solar wind speeds and found that the majority of vortices are consistent with a KH instability origin. KH vortices in the large plasma device experiment have been probed and characterized by an array of Langmuir probes (Horton et al., 2005). In addition, vorticity may be important in studies of turbulence (e.g., Consolini et al., 2015), magnetic reconnection (e.g., Phan et al., 2016), and plasma heating (e.g., Parashar & Matthaeus, 2016).

Due to the fact that the scale size of structures of interest should be much larger than that of the spacecraft tetrahedron, the Cluster mission (interspacecraft separation between 100 km and 18,000 km) is suitable for macrophysics of magnetohydrodynamics, whereas the MMS (interspacecraft separation between 10 km and 400 km) is suitable for microphysics of plasma kinetic theory. For techniques that resolve geometrical parameters such as MCA, tetrahedron size impact should be discussed. The robustness of four-spacecraft methods is dependent on size, elongation, and planarity of the tetrahedron shape, quantified as the so-called "tetrahedron geometrical factors" by Robert et al. (1998). Since the gradient estimation is based on a first-order approximation, for example, assuming the physical linearity, the relative error increases as the tetrahedron size becomes bigger. Tetrahedron size impacts have been studied in various four-spacecraft tools such as the *k* filtering technique for plasma turbulence studies (Sahraoui et al., 2010) and the first-order Taylor expansion for finding magnetic nulls (Fu et al., 2015). Highly irregular shapes of tetrahedron (e.g., almost planar or

highly elongated) result in large errors (>10%) of the current density (Robert et al., 1998), as estimated from the curlometer technique (Dunlop et al., 1988).

We propose to combine four-spacecraft techniques for magnetic curvature and vorticity analyses in KH studies. We first present a resistive MHD simulation of KH waves at the Earth's flank magnetopause in section 2 and then the application of the four-spacecraft analyses in section 3. The spatial studies in section 4.1 and temporal studies in section 4.2 are done using virtual spacecraft at typical Cluster scale sizes. These studies provide the basis for sketching local magnetic field and flow geometries around a spacecraft trajectory. Effects of the varying spacecraft tetrahedron size are examined in the spatial studies in order to test the robustness of the methods. We finally summarize and discuss potential applicability of MCA and vorticity techniques in section 5.

2. Simulation

We simulate the Kelvin-Helmholtz instability using Lare2d, a Lagrangian-step resistive MHD code with a staggered grid in 2.5-D (Arber et al., 2001). The simulation reproduces Kelvin-Helmholtz waves for typical conditions along the Earth's flank magnetopause on the duskside.

Normalization values are the following. The normalization length $L_0 = 600$ km, time $t_0 = 4$ s, the speed $v_0 = L_0/t_0 = 150$ km s^{-1}. The normalization ion density $n_0 = 10$ cm^{-3}, magnetic field $B_0 = v_0\sqrt{\mu_0 n_0} = 21.7$ nT, and temperature $T_0 = 2.7 \times 10^6$ K.

The simulation box is of the size $80 \times 40\ L_0^2$, which corresponds to $7.5 \times 3.8\ R_E^2$. The grid resolution is $N_x \times N_y = 320 \times 160$; hence, each cell covers $L_0/4 \times L_0/4$ km^2. The XY plane of the simulation represents the equatorial-GSM plane with the X axis directed sunward. The simulation domain is periodic in the X direction and open in the Y direction.

Let the subscripts 1 and 2 represent magnetosheath and magnetospheric sides, respectively. The parameter profiles are given by

$$n = (n_1 + n_2)/2 + (n_1 - n_2)\tanh[(y - y_0)/\Delta w])/2 \quad (1)$$

$$B = (B_1 + B_2)/2 + (B_1 - B_2)\tanh[(y - y_0)/\Delta w])/2 \quad (2)$$

$$T = (T_1 + T_2)/2 + (T_1 - T_2)\tanh[(y - y_0)/\Delta w])/2 \quad (3)$$

$$V = -V_1(\tanh[(y - y_0)/\Delta w] + 1)/2, \quad (4)$$

where y_0 is the midplane Y position and $\Delta w = L_0$ is the width of the boundary layer. The boundary layer and current sheet are centered and colocated for simplicity. The initial simulation parameters are the magnetic field strength $B_1 = B_2 = 0.92B_0$, ion density $n_1 = n_0, n_2 = 0.1n_0$, ion speed $V_1 = 2.0v_0$, and temperature $T_1 = 0.85T_0, T_2 = 9.8T_0$. Note that the temperature T is not a free parameter and it must be calculated to balance the total plasma and magnetic pressures at the midplane. The flow velocity $\mathbf{V} = (V, \delta V, 0)$ is initially defined mainly in the X direction with a small transverse perturbation in the Y direction. The KH wavelength is defined by the initial sinusoidal perturbation δV, which is a half of the box length ($\lambda_{KH} = 40L_0$). The initial magnetic field is given by $\mathbf{B} = B(\sin\varphi, 0, \cos\varphi)$, $\varphi = 10°$, making an angle of $90° - \varphi$ with the main flow direction.

Physically, the simulated KH event lasts $150t_0 = 600$ s, with a repetition period of $25t_0 = 100$ s (frequency 10 mHz). The wave phase speed is 241 km s^{-1}. This is between the linear theory prediction of KH wave group speed that is the boundary center of mass velocity $\mathbf{V}_{cm} = (n_1\mathbf{V}_1 + n_2\mathbf{V}_2)/(n_1 + n_2) = 273$ km s^{-1} and the average velocity $\mathbf{V}_{avg} = (\mathbf{V}_1 + \mathbf{V}_2)/2 = 150$ km s^{-1}, consistent with the prediction of KH wave speed for a finite-thickness shear layer (Hasegawa et al., 2009). The KH wavelength is 3.7 R_E, consistent with observed events where the KH wavelengths vary from a few R_E to ~10 R_E (e.g., Lin et al., 2014; Taylor et al., 2012). We analyze up to six back and forth boundary motions of this wave from linear to nonlinear stages.

3. Four-Spacecraft Analyses

We set up virtual probes in a regular tetrahedron configuration and vary the separation size $a = L_0/4, L_0/2, \ldots,$ up to $12L_0$ in the simulation. The virtual probes are labeled by SC1, SC2, SC3, and SC4 with the barycenter

in the simulation plane. Note that we have assumed some translation/duplication of the 2-D plane in the *Z* direction. This is justified with the KH wave because the wave is perturbed in the *Y* direction, not in the *Z* direction.

To calculate the magnetic curvature, we expand $\mathbf{C} = \mathbf{b} \cdot \nabla \mathbf{b}$, where $\mathbf{b} = \mathbf{B}/|\mathbf{B}|$, into

$$C_j = B^{-2} \sum_i B_i G_{ji} - B^{-4} B_j \sum_{i,k} B_i B_k G_{ki}, \quad i,j,k \in x,y,z \tag{5}$$

as in Shen et al. (2003), where $B_i = \sum_{\alpha=1}^{4} B_{\alpha i}/4$ are average magnetic field components from four-spacecraft ($\alpha = 1, 2, 3, 4$) and $G_{ij} = \partial_j B_i$ are magnetic field gradient tensors. The magnetic field gradient tensors are composed of two parts $G_{ij} = G^0_{ij} + \lambda R^{-1}_{ij}$, where the local magnetic gradient tensors (G^0_{ij}) are corrected with the solenoidal constraint ($\nabla \cdot \mathbf{B} = 0$) through the Lagrangian multiplier $\lambda = -G^0_{ii}/R^{-1}_{ii}$, where the volumetric tensors $R_{ij} = \sum_{\alpha=1}^{4} r_{\alpha k} r_{\alpha_j}/4$, for given position vectors $\mathbf{r}_\alpha$ of spacecraft α. In our work, we apply the barycentric method for calculating magnetic gradient tensors $G^0_{ij} = \sum_{\alpha=1}^{4} B_{\alpha i} k_{\alpha j}$, where the reciprocal vectors $\mathbf{k}_\alpha = (\mathbf{r}_{\beta\gamma} \times \mathbf{r}_{\beta\lambda})/(\mathbf{r}_{\beta\alpha} \cdot \mathbf{r}_{\beta\gamma} \times \mathbf{r}_{\beta\lambda})$, $\mathbf{r}_{\alpha\beta} = \mathbf{r}_\beta - \mathbf{r}_\alpha$ are relative position vectors and $(\alpha, \beta, \gamma, \lambda)$ must be a cyclic permutation of $(1, 2, 3, 4)$. Results of the method are subject to a truncation error from Taylor's expansion, which is of order $(a/D)^2$, where a is the spacecraft separation and D is the scale size of the structure of interest. Note that a relative error a/D to the first order is also used in the literature. We have benchmarked our MCA code against published literature both in Cluster and MMS data.

To calculate the vorticity $\mathbf{\Omega} = \nabla \times \mathbf{V}$, we apply the linear barycentric estimator of curl of vector field given in Chanteur (1998) as $\mathbf{\Omega} = \sum_{\alpha=1}^{4} \mathbf{k}_\alpha \times \mathbf{V}_\alpha$. This estimator does not enforce the solenoidality of the vector field, which is desirable for our compressible fluid ($\nabla \cdot \mathbf{V} \neq 0$). Errors of the method were explicitly derived by Vogt and Paschmann (1998) depending on instrumental errors. These errors were found to be less than 12% for cross products of velocity (Gurgiolo et al., 2010).

A tetrahedron of virtual spacecraft scale size $a = 4L_0$ (MHD scale) is used for reproducing spatial profiles along the spacecraft trajectory, equivalent to KH observations along the wave propagation direction, and temporal profiles equivalent to observed time series by a spacecraft sampling the plasma. For greater visualization, 2-D *XY* maps are constructed at a given time from combining multiple spatial *X* profiles together across the *Y* range. These maps constructed from point-by-point measurements are helpful to give a full picture of the curvature and vorticity *in the simulations for this study*, which is informative to understand observational data of KH waves (a first step for future works using real data). The single-spacecraft proxy for identifying rolled-up KH vortices so-called "lower-density-faster-than-sheath (LDFTS) plasma" (Takagi et al., 2006) is revisited in order to compare and to identify the stages of vortex development.

4. Results

4.1. Spatial Studies

Figure 1 shows the spatial profiles of the selected snapshot ($t = 100t_0$) for the nonlinear KH waves exhibiting fully rolled-up vortices. Figure 1a shows the virtual spacecraft by the four yellow points forming a regular tetrahedron configuration of side length $a = 4L_0$ with the path of its barycenter flying across KH vortices (shown in ion density). To describe general properties along the trajectory, we mark six vertical gray dashed lines by numbers (1)–(6). The yellow box outlines the region of width $1\lambda_{KH} = 40L_0$ for later analyses. The vortex regions, that is, between (2) and (4), show tenuous ion density from the magnetospheric side in Figure 1b, with a local increase of midvalue density (between the magnetosheath and magetospheric values) at (3), as seen by SC1 and SC4. This vortex region also shows a local drop in magnetic field component B_z at around (3) in Figure 1c. The total pressure in Figure 1d reaches its maximum around the wave trailing edges, that is, between (5) and (6), and reaches its minimum in the vortex center at around (3). The ion velocity is two dimensional, giving the vorticity component Ω_z shown in Figure 1e, which reaches its maximum around the vortex center (3). The magnetic curvature radius $R_c = 1/|\mathbf{C}| = 1/\sqrt{C_x^2 + C_y^2 + C_z^2}$ in Figure 1f drops to a value of about a half wavelength around the vortex center (3). The magnetic curvature in Figure 1g shows approximately zero curvature at (1) and (4), which corresponds to magnetic field lines perpendicular to the plane ($B_x = B_y \approx 0$ in Figure 1c). The leading edge of the rolled-up vortex at (2) shows a positive peak in C_y. The vortex center (3) shows negative C_x, which apparently gives rise to the small curvature radius in this region. The wave trailing edge between (5) and (6) shows magnetic rotation, marked by a reverse direction of all curvature components. Table 1 notes explicitly the curvature radius, magnetic curvature, and magnetic field values at locations (1)–(6).

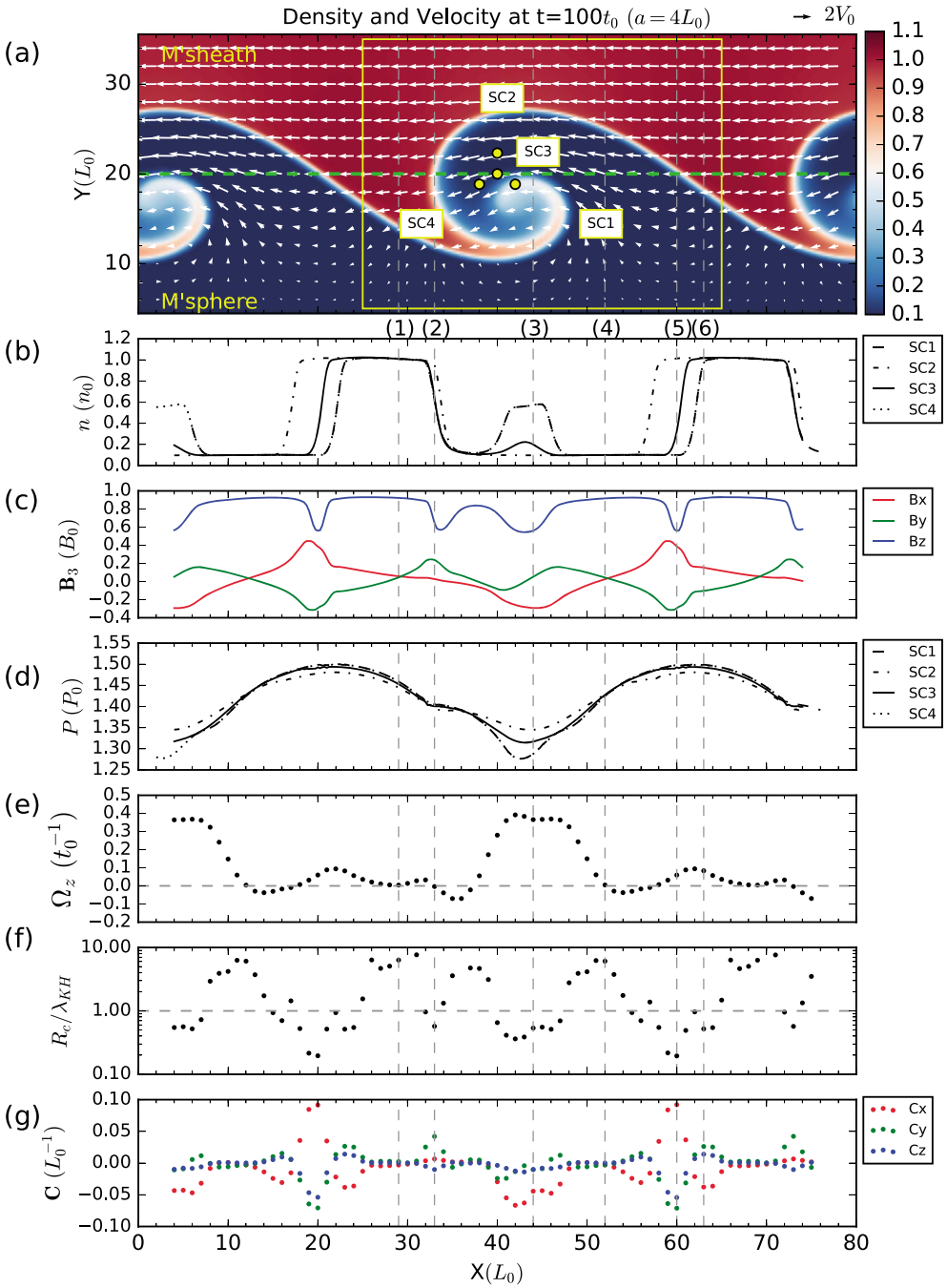

Figure 1. Spatial profiles of the nonlinear KH waves. (a) KH vortices shown in ion density, overplotted by velocity field (white vectors), with the four-spacecraft configuration of a regular tetrahedron of side length $a=4L_0$ (yellow dots) (SC1 (right), SC2 (top), SC3 (middle), and SC4 (left)) and the spacecraft trajectory (green dash) through the midplane. The following panels are parameter profiles along the spacecraft trajectory shown in Figure 1a. (b) Ion density at SC1–SC4, (c) magnetic field at SC3, (d) total pressure at SC1–SC4, (e) flow vorticity, (f) magnetic curvature radius, and (g) curvature vector components. The yellow box in Figure 1a outlines the region for analyses in Figures 5 and 7.

In Figure 2, we sketch schematic 3-D magnetic field lines threading through the KH waves at the equatorial plane based on the values in Table 1. The simulated magnetic fields are shown in the equatorial plane $Z=0$ in GSM coordinates, where B_z is shown in gray scale and B_x, B_y are shown as streamlines. The following sketch is consistent with the associated field line orientations (not shown) and is drawn in a magnetospheric context. Considering that the magnetic field lines are straight initially and connected to the high latitudes

Table 1
Magnetic Curvature and Field Values at the Marked X Positions

	X positions	R_c/λ_{KH}	$\mathbf{C}(L_0^{-1})$	$\mathbf{B}_3(B_0)$
(1)	29	6.0	(0.00, 0.00, 0.00)	(0.06, 0.05, 0.92)
(2)	33	0.6	(0.01, 0.04, −0.01)	(0.03, 0.24, 0.65)
(3)	44	0.6	(−0.04, −0.01, −0.01)	(−0.29, 0.05, 0.56)
(4)	52	6.0	(0.00, 0.00, 0.00)	(0.06, 0.05, 0.92)
(5)	60	0.2	(0.09, −0.07, −0.05)	(0.39, −0.29, 0.56)
(6)	63	0.5	(−0.04, 0.03, 0.01)	(0.15, −0.10, 0.92)

Note. From tetrahedron size $a = 4L_0$. (See Figure 1.)

(in the Northern and Southern Hemispheres, which are more stable to KH instabilities), 3-D magnetic field lines may be drawn as follows. Zero curvatures at (1) and (4) in Table 1 correspond to straight magnetic field lines in the magnetosheath (red field line at (1) in Figure 2) and magnetospheric (blue field line at (4) in Figure 2) sides, respectively. Curvature at (2) that is dominant in positive C_y, with a radius value of $R_c = 0.6\lambda_{KH}$, corresponds to the purple field line at (2) in Figure 2. Magnetic curvature at this location (shown by green vector) indicates magnetic tension at the boundary layer against the counterclockwise twist (seen from above) of the vortex. Curvature at (3) that is dominant in negative C_x, with a radius value of $R_c = 0.6\lambda_{KH}$, corresponds to the purple field line at (3) in Figure 2. Magnetic field line at (3) is consistent with a sweep, possibly of a pristine magnetic field line at location (2), counterclockwisely into the inner part of the vortex. Curvature radius at (5) is very small, with a value of $R_c = 0.2\lambda_{KH}$, due to a strong perturbation in magnetic curvature in all directions. The region (5) is called "KH spine" in Otto and Fairfield (2000) (and also in Miura, 1984, 1987; Wu, 1986), which is characterized by a strong reduction of B_z and typical extrema in B_x, B_y with opposite polarity. Magnetic curvature in this region points in positive X direction and negative Y direction as indicated by a green vector at (5), consistent with the dragging of plasma along the boundary region into the vortex. Magnetic curvature at (6), in contrast, points in the opposite direction to that of (5) with a smaller curvature magnitude (larger curvature radius). From (5) to (6), the magnetic field rotates by ~180°, presumably due to different inertia on both sides of the boundary layer (with higher inertia on the magnetosheath side due to denser ion population). We then investigate the tetrahedron size effects in details at the locations (2), (3), and (5) as follows.

We apply the MCA and vorticity techniques using tetrahedrons of varying sizes and with their barycenters located at three different positions in the KH vortex. Figure 3 shows curvature radius (a–c), curvature direction (d–f), and vorticity magnitude (g–i). The values for the leading (a, d, g), inner (b, e, h), and trailing edges (c, f, i)

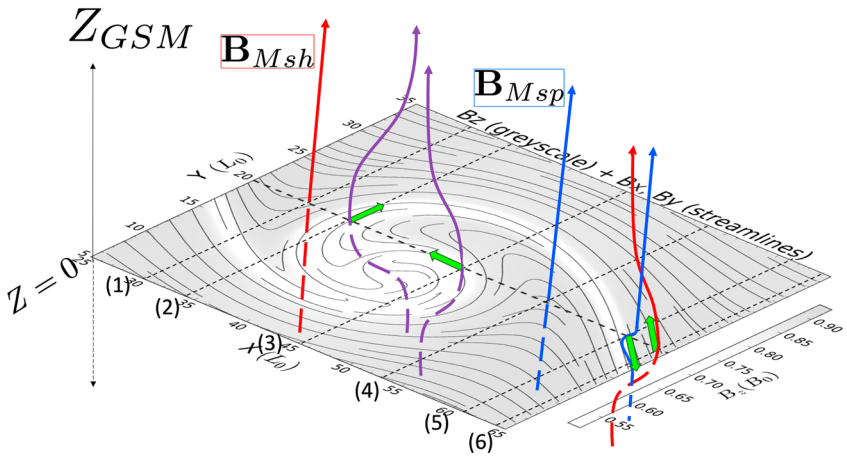

Figure 2. A schematic magnetic field of KH vortex. The simulation plane at $Z = 0$ (in GSM coordinates) shows magnetic field components B_z in gray scale and B_x, B_y with streamlines. Three-dimensional magnetic field lines are inferred based on magnetic curvature and curvature radius at locations (1)–(6) as marked in Figure 1 (see Table 1). Blue, red, and purple lines depict the field lines from magnetospheric (Msp), magnetosheath (Msh), and boundary layer regions, respectively. Green vectors represent magnetic curvature as resolved in the equatorial plane.

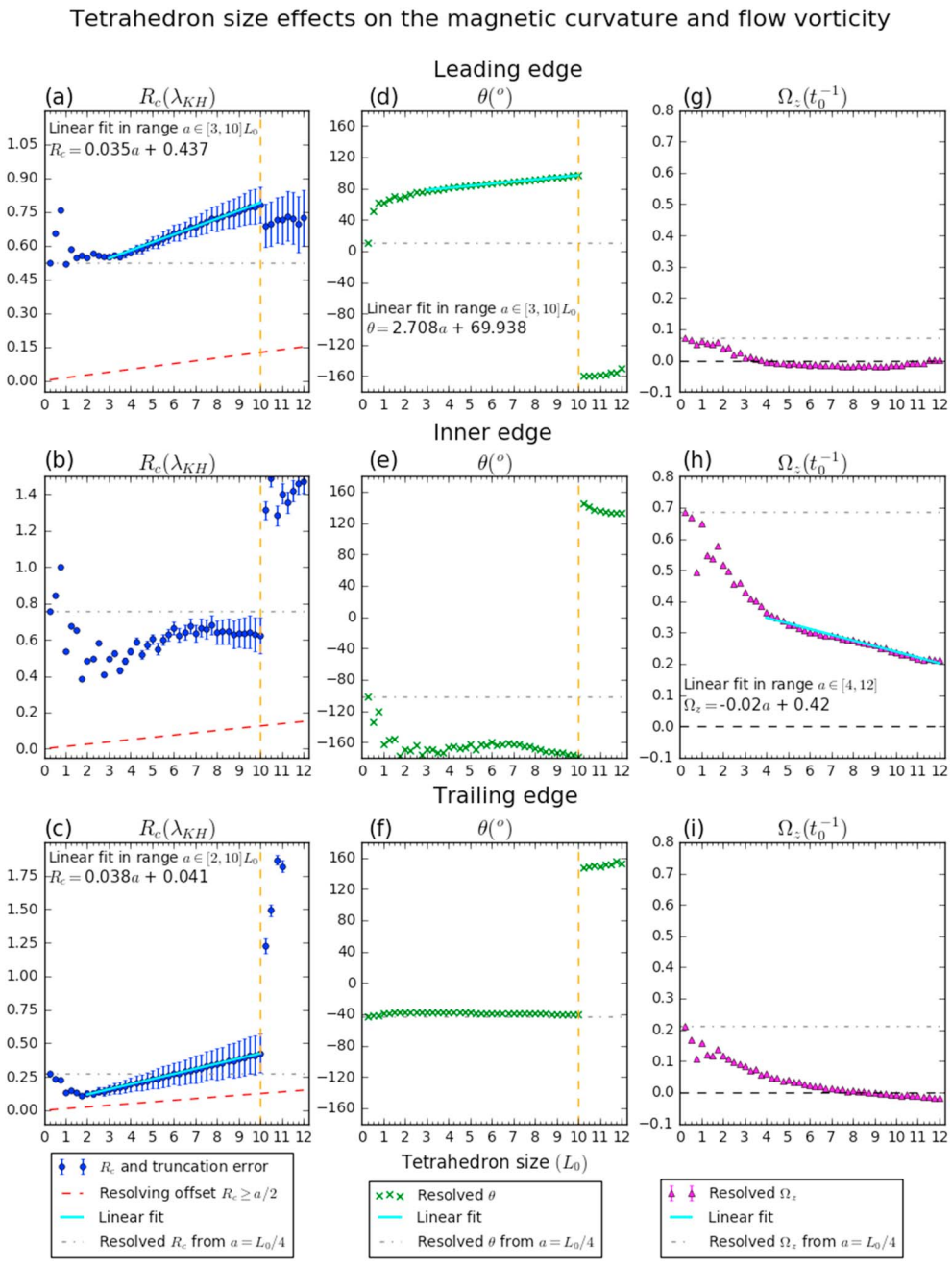

Figure 3. Curvature radius (a–c), curvature direction (d–f), and vorticity (g–i) against tetrahedron sizes at the selected locations : leading edge (Figures 3a, 3d, and 3g), inner edge (Figures 3b, 3e, and 3h), and trailing edge (Figures 3c, 3f, and 3i) of the KH vortex shown in Figure 2 (numbers (2), (3), and (5), respectively).

of the KH vortex are shown at the locations (2), (3), and (5), respectively of Figure 2. The values for $a = L_0/4$ are represented with the horizontal gray dash-dotted lines. Truncation errors of order $(a/D)^2$ are represented with error bars in blue. In addition, to be resolved, the structure scale must be larger than a half of the spacecraft separation $R_c \geq a/2$ (Shen et al., 2003), denoted here as a "resolving offset." The validity of curvature radius data is represented by results above the resolving offset (shown as red dashed lines). Despite the truncation error bars, the results show that the resolved curvature radius increases with the tetrahedron size, linearly in range from a few L_0 to $10L_0$ particularly for the leading and trailing edges. The curvature direction does not change much in the same range. Vertical orange dashed lines denote the break in the linear increase at the tetrahedron size $10L_0$. Both curvature radius and direction erratically vary outside the "linear" range,

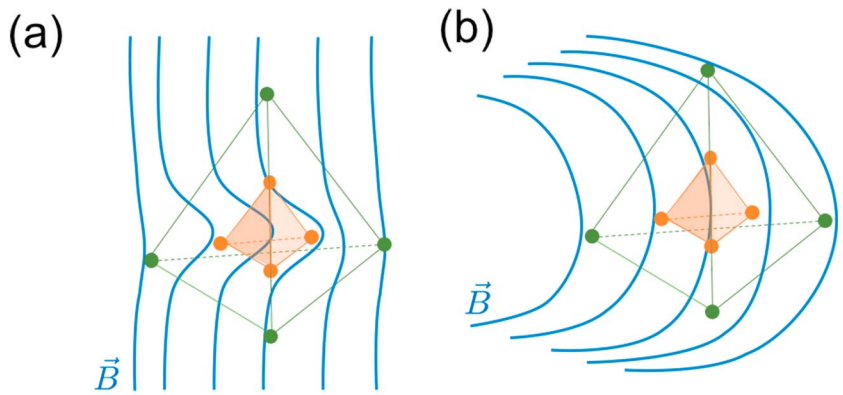

Figure 4. Spatial variations in magnetic field structures (blue) measured by nested spacecraft tetrahedrons of small (shaded orange) and large (green) scales (with the same barycenter). The magnetic field structures have (a) no variation at large scales but "kinked" in the small scale and (b) no variation at the small scale but with linear gradient at large scale. As the tetrahedron size increases, these two physical structures would lead to increasing (Figure 4a) and decreasing (Figure 4b) variations in radius of curvature.

presumably because the magnetic fields do not have much linearity in the small ($\lesssim 3L_0$) or large ($>10L_0$) scales. The vorticity magnitude in Figures 3g–3i generally decreases as the tetrahedron size increases. This shows that the vorticity gradients of the KH wave are spatially quite constant, with strong vortical flows at the smaller scale; that is, in Figure 3h, we find that the linear fit $\Omega_z = -0.02a + 0.42$ in the range of tetrahedron sizes $a \in [4, 12]$.

The linear or nonlinear variations in the four-spacecraft results with respect to the tetrahedron size could arise from spatial variations in the physical structures or from limitations in the techniques themselves. In Figure 4, we illustrate how spatial variations in the physical structures may lead to variations in curvature by considering two possible scenarios. For both of these scenarios, we cannot regard the variations of the curvature with respect to the tetrahedron size as inaccuracy of the technique but rather the nonlinearity of the physical structures. Similar considerations would apply for the vorticity. To fully understand the magnetic curvature of the KH wave, we further apply the MCA at every Y location and then construct magnetic curvature maps. Figure 5 shows a comparison of the magnetic curvature maps of a fully rolled-up vortex from three sizes of tetrahedron ($a = L_0/4, L_0, 4L_0$). Figure 5 (left column) shows the curvature radius R_c in wavelength unit, and Figure 5 (right column) shows the curvature direction $\theta = \arctan(C_y/C_x)$ from 0° to 180° and 0° to −180°, overplotted with the curvature projection $\mathbf{C}_p = C_x\mathbf{i} + C_y\mathbf{j}$. We will first investigate the curvature from the smallest tetrahedron and then study the effects of tetrahedron size.

We may characterize vortex regions based on magnetic curvature from the smallest tetrahedron ($a = L_0/4$) as it gives the least truncation error $O \sim (a/R_c)^2$ in Figure 5a. Curvature radius (left column) shows increasing values away from the magnetopause as delineated by black dots. One most prominent feature is the region of low curvature radius, of order $0.1\lambda_{KH}$ (red) to $0.5\lambda_{KH}$ (green), on the magnetospheric side of the magnetopause. In this region, labeled by [1] in the right panel, hereafter referred to as "magnetospheric (M'spheric) KH spine," possesses θ directed from −45° to 45° (antiwave propagation direction) shown as a mint green patch. On the magnetosheath side of the magnetopause, labeled by [2] in the right panel, hereafter referred to as "magnetosheath (M'sheath) KH spine," in contrast, is observed and possesses θ directed from 90° to 180° (wave propagation direction) shown as an orange-red patch. The curvature direction surrounding the rolled-up magnetopause on the magnetospheric side, labeled by [3] in the right panel, hereafter referred to as "magnetospheric (M'spheric) vortex," gradually increases from 45° (golden) to 180° (red) and then −180° (purple) to −45° (blue) with respect to the vortex rotation (anticlockwise seen from above). A similar pattern can be noticed next to the magnetopause on the magnetosheath side, labeled by [4] in the right panel, hereafter referred to as "magnetosheath (M'sheath) KH vortex," where θ increases from −180° (purple) to 90° (golden). In the vicinity of the vortex center, labeled by [5] in the right panel, the curvature radius varies from $0.5\lambda_{KH}$ (green) to $9.0\lambda_{KH}$ (navy blue). Curvature in this region, delineated by gray dashed lines, points in all directions except from −45° to 45°. Table 2 summarizes these characteristic regions. For a temporal evolution of these characteristic regions, see Movie S1 in the supporting information. Figure 6 is adapted from Figure 5a to sketch these regions based on the values in Table 2.

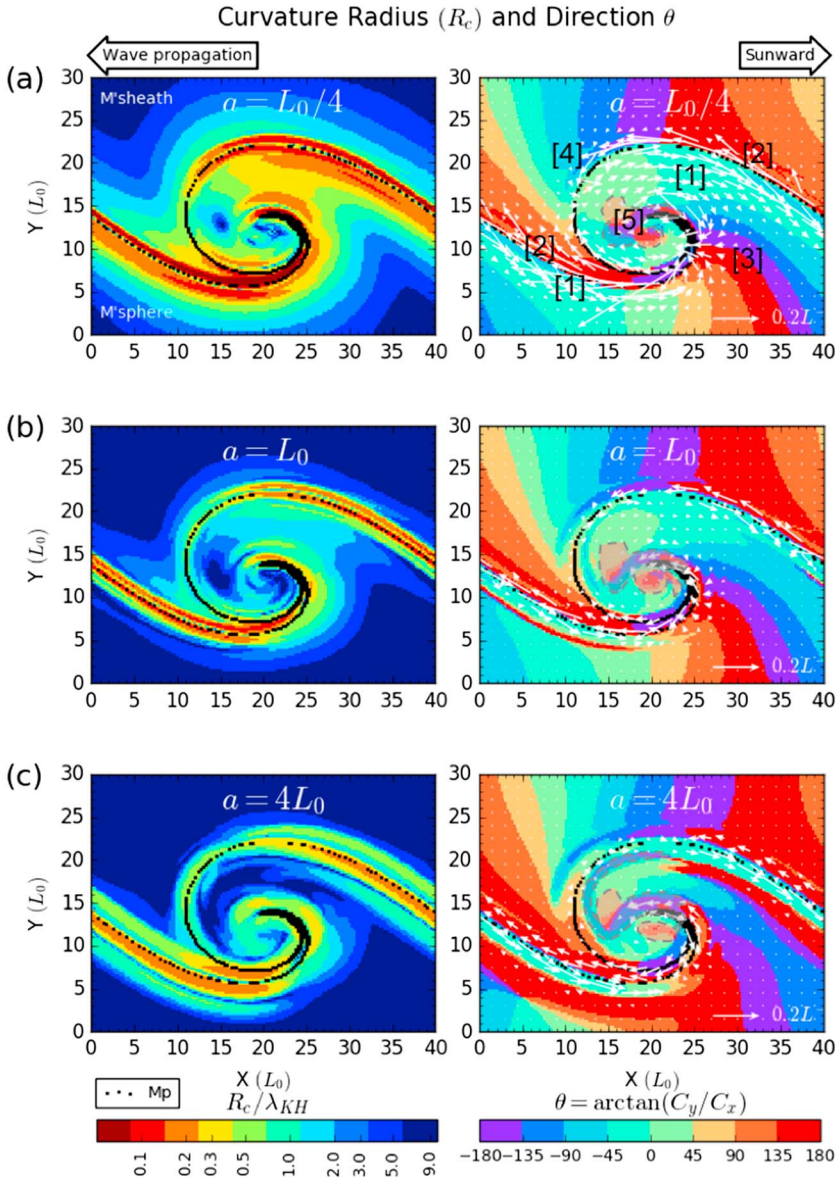

Figure 5. Magnetic curvature of a fully rolled-up KH vortex. Curvature is calculated from the MCA algorithm with tetrahedron sizes (a) $a = L_0/4$, (b) $a = L_0$, and (c) $a = 4L_0$. Curvature radius is shown in the left column in discrete color (nearest interpolation). Curvature direction is shown in the right column with values binned to 45° range. White vectors in the right column represent curvature projection. Numbers in the top right panel label the vortex regions [1] magnetospheric KH spine, [2] magnetosheath KH spine, [3] magnetospheric vortex, [4] magnetosheath vortex, and [5] vortex center. (See Table 2.) Shaded areas outlined by gray dashed lines in the right column mark vortex center regions. For a temporal evolution of the top right panel, see Movie S1 in the supporting information.

Table 2
KH Vortex Region Characterization

Regions	Range of θ	Range of R_c/λ_{KH}
[1] Magnetospheric KH spine	$-45° \le \theta \le 45°$	0.1–0.5
[2] Magnetosheath KH spine	$90° \le \theta \le 180°$	0.1–0.5
[3] Magnetospheric vortex	$45° \le \lvert\theta\rvert \le 180°$	0.5–2.0
[4] Magnetosheath vortex	$-180° \le \theta \le 90°$	0.5–2.0
[5] Vortex center	$45° \le \lvert\theta\rvert \le 180°$	0.5–9.0

Note. From tetrahedron size $a = L_0/4$. (See Figures 5a and 6.)

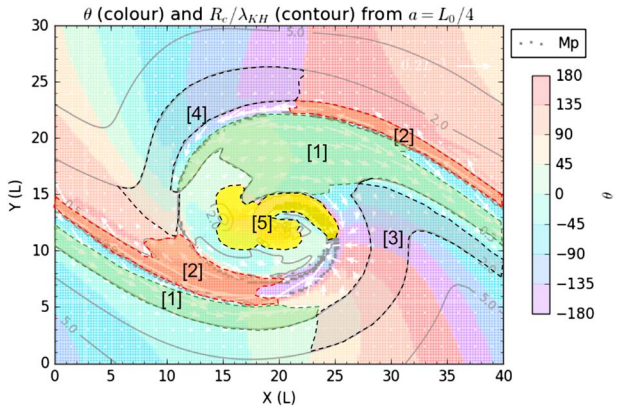

Figure 6. Sketch of the characteristic KH vortex regions adapted from Figure 5a. Dashed lines mark boundaries of the characteristic regions using the criteria in Table 2.

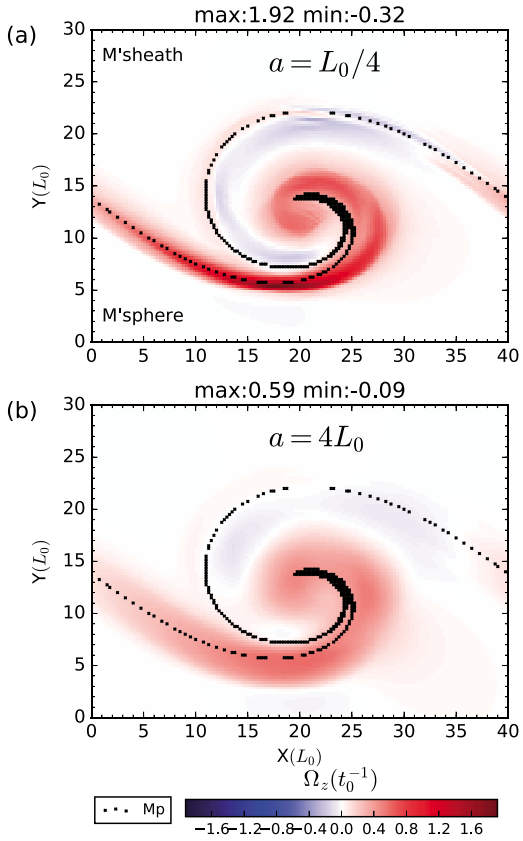

Figure 7. Flow vorticity of a fully rolled-up KH vortex. Vorticity component Ω_z is calculated from vorticity technique with tetrahedron sizes (a) $a = L_0/4$ and (b) $a = 4L_0$. Magnitude of vorticity is shown in symmetric color scale from red (positive) to blue (negative). The negative vorticity, sandwiched between the vortex core and the magnetopause, is explained by the rolling-up process in which the vortex core has a stronger (positive) vorticity than the outer vortex regions near the magnetopause (original shear layer) (see text).

We now investigate the impact of the tetrahedron size on magnetic curvature in Figure 5. In the vicinity of the KH vortex, the smaller tetrahedron yields more pronounced drops in radius values (see Figure 5a in comparison to Figures 5b and 5c). Curvature radius from bigger tetrahedron increases faster away from the magnetopause. Curvature direction from bigger tetrahedron resembles pattern from smaller tetrahedron but with less defined outline. Magnetospheric KH spine (labeled by [1] in Figure 6) is clearly visible in cases $a = L_0/4$ and $a = L_0$. Magnetosheath vortex pattern (labeled by [4] in Figure 6) persists for all tetrahedrons; however, magnetospheric vortex (labeled by [3] in Figure 6) appears less distinct as tetrahedron size increases. The mix of curvature direction identified at vortex center in right panel (in shaded area delineated by gray dashed lines) from bigger tetrahedron appears less clustered. This suggests that only some characteristic regions such as magnetospheric KH spine and magnetosheath vortex can be resolved by MCA across all tetrahedron sizes, at least up to $a = 4L_0$ ($0.1\lambda_{KH}$).

Figures 7a and 7b show a comparison of vorticity from the tetrahedron sizes $a = L_0/4$ and $a = 4L_0$, respectively. Flow vorticity dominates around the magnetopause, as expected for an original shear layer. Flow vorticity peaks at the same locations for both tetrahedron sizes, but the magnitude is weaker for the bigger tetrahedron. This can be explained by the scaling of vorticity magnitude $|\Omega_z| = |\nabla \times V| \sim (V_2 - V_1)/a$, which reads that the magnitude of vorticity is inversely proportional to the interspacecraft separation a, for constant asymtotic values V_1 and V_2. However, this scaling is only satisfied when the spacecraft separation a is big enough (larger than the width of shear layer Δw) to sample the velocities on both sides of the shear layer. The vorticity is dominantly positive in and around the vortex center, associated with counterclockwise rotation of KH vortex seen from above. This is consistent with vortical flow motion expected on the duskside magnetopause. However, there is a small negative vorticity in the magnetospheric side of the magnetopause, which may be attributed to a small clockwise rotation flow. We will further investigate this negative vorticity in the temporal studies.

4.2. Temporal Studies

Figure 8 shows time series for static spacecraft in the boundary layer recorded at the simulation center (probe positions in Figure 1a) using tetrahedron size $a = 4L_0$ from the time $t = 20t_0$ to $t = 240t_0$ of the simulation. Note that the tetrahedron size $a = 4L_0$ (MHD scale), as illustrated in the spatial studies, is in the range in which the dependence on the tetrahedron size is linear. The time snapshot (in density) at $t = 100t_0$ in Figure 1 and time snapshots (in vorticity) at $t = 88t_0$, $122t_0$ and $160t_0$ in Figure 10, which we will later discuss, are used to illustrate various stages of the KH wave. Ion density in Figure 8a recorded at the four probes shows six back and forth motions of the boundary layer during the time $t = 50t_0 - 200t_0$. We mark six transits from the magnetosphere to magnetosheath with numbers (1)–(6). Magnetic field at SC3 in Figure 8b shows opposite polarity peaks of B_x and B_y, which coincide with drop in B_z, showing characteristics of KH spines at the marked transits. Figure 8c shows ion velocity fluctuations at SC3. It is useful to note that a region of LDFTS is present between transits (2) and (3). Total pressure in Figure 8d shows maxima at the transits (1)–(3). Curvature components in Figure 8e shows a clear reversal in direction of C_x while crossing from the magnetosphere to magnetosheath. Curvature radius in Figure 8f is found to be decreasing with time and reaching a value of less than a half wavelength $R_c \sim 0.5\lambda_{KH}$ at transit (2) ($t = 88t_0$). The curvature radius stays low after the transit (2) and fluctuates around the value of one wavelength until reaching the transit (5), then it fluctuates around increasing values between $\sim 0.5\lambda_{KH} - 10\lambda_{KH}$. Curvature

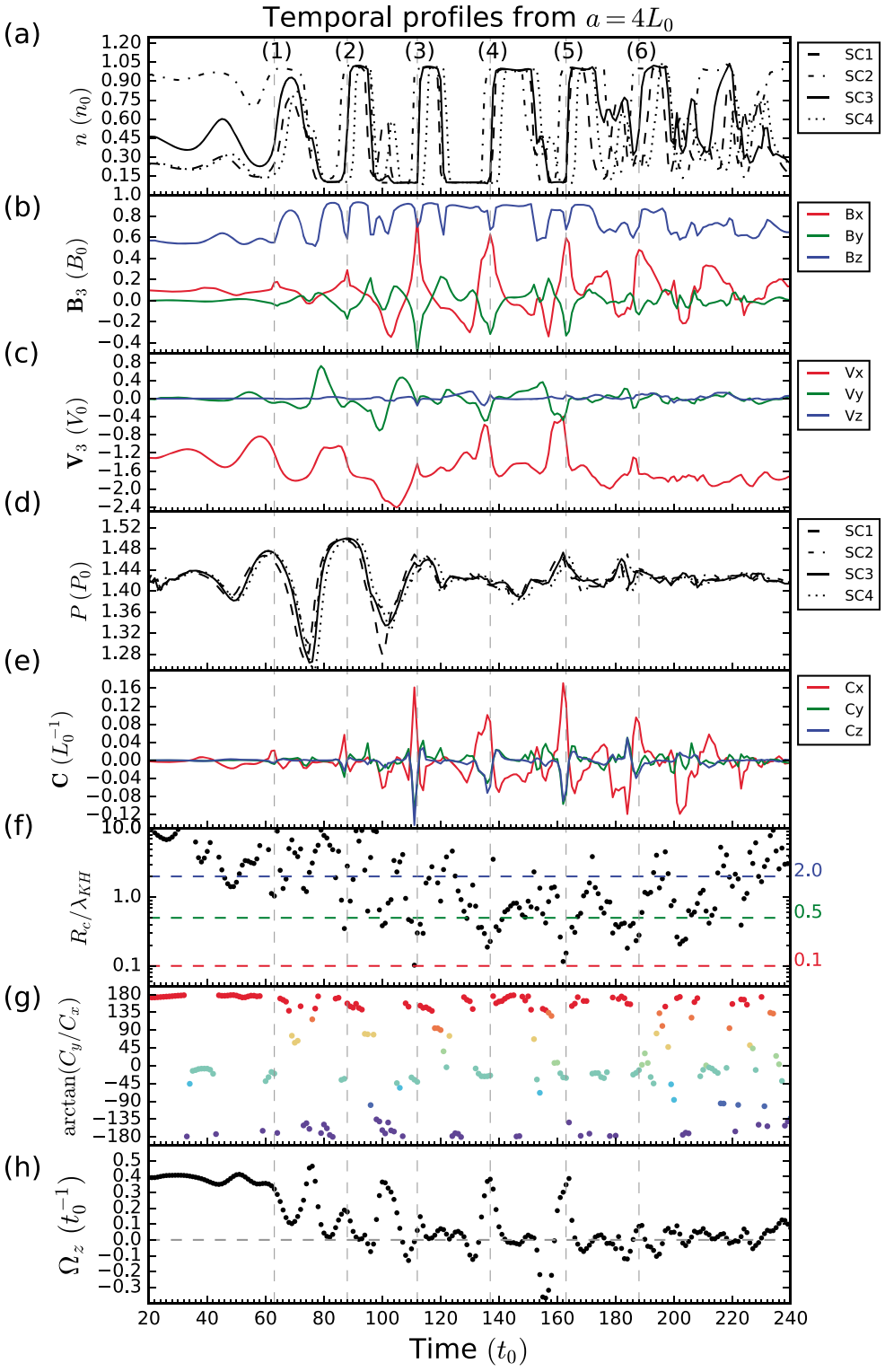

Figure 8. Time series from the tetrahedron size $a = 4L_0$ with the barycenter at SC3 in Figure 1. (a) Density at SC1–SC4, (b) magnetic field at SC3, (c), ion velocity at SC3, (d) total pressure at SC1–SC4, (e) curvature components, (f) curvature radius, (g) curvature direction, and (h) flow vorticity. Numbers and vertical dashed lines mark transits from magnetosphere to magnetosheath. Curvature direction in Figure 8g is color coded to correspond with the right column of Figure 5.

direction (color coding corresponds to curvature direction in Figure 5) in Figure 8g changes from ~0° (mint green dots) to ~180° (red dots) during the transitions. Vorticity in Figure 8h starts out at the value $\Omega \approx 0.4t_0^{-1}$ because the probe barycenter is initially at the center of the original shear layer. There are two clear peaks of vorticity between the transits (1) and (3) that are colocated with minimum in total pressure, as expected for rolled-up KH vortices at $t = 76t_0$ and $t = 100t_0$. Brief episodes of negative vorticity are detected after the transits (2)–(6), and the vorticity peaks afterward when the probes are crossing the KH spines (4)–(6). While the LDFTS is expected away from the vortex core in the magnetospheric side of the rolled-up vortex (Hasegawa et al., 2006), it is not always present in the time series. On the other hand, the negative vorticity is present after the vortex has rolled-up. The negative vorticity, generated during the rolling-up process, can be explained by the radial distributions (horizontal cuts) of the ion density and vorticity away from the vortex center as seen in Figures 1b and 1e. Here the inner denser part of the vortex core (e.g., number (3) as reference) rotates faster than the outer tenuous part (number (4)), which is of magnetospheric origin. Since this tenuous part has zero vorticity initially and is between a strong positive vorticity of the vortex core (number (3)) and a weaker positive vorticity of the outer vortex regions near the magnetopause (original shear layer) (number (5)), it is susceptible to a reversed flow direction (see Figure 8c) and therefore causing the negative vorticity. This effect is also clearly seen in Figure 7 and Movie S2 in the supporting information.

To understand the time evolution in the latter quantities in Figure 8, the analyses are done as follows. First, we take a time snapshot in KH vortex frame in the X range of one wavelength (see the yellow box in Figure 1a) for total pressure, curvature radius, and vorticity. Three Y locations at the midplane (Y_{mid}), on the magnetosheath side ($Y_{mid} + \lambda_{KH}/8$), and on the magnetospheric side ($Y_{mid} - \lambda_{KH}/8$) are chosen, as marked by green, orange, and blue dashed lines, respectively, in Figure 10. For each quantity, we calculate the difference between its minimum value and maximum value at a given Y location. This is a useful indicator of the level of the KH activity over time. To refer to evolution of the KH wave, we calculate KH growth from the average velocity perturbation of the whole simulation. To apply the LDFTS proxy, we calculate the percentage of roll-up (% RO) as in Taylor et al. (2012). The lower-density $n < 0.7n_{max}$ and faster-than-sheath $V_x < \langle V_x \rangle - \sigma$ criteria, where n_{max} is the maximum density, $\langle V_x \rangle$ is the average ion velocity of the time series, and σ is the standard deviation, are set as threshold for LDFTS plasma. The maximum density n_{max} and the average ion velocity $\langle V_x \rangle \pm \sigma$ are obtained from Figures 8a and 8c, respectively. Figure 9 shows (a) KH growth, (b) % RO, (c) change in pressure ΔP, (d) change in curvature radius ΔR_c, and (e) change in vorticity $\Delta\Omega_z$ as a function of time.

The KH growth rate in Figure 9a shows one growing mode with nonlinear stage during $t = 40t_0 - 120t_0$. Figure 9b shows nonzero % RO during around $t = 80t_0$ to around $t = 122t_0$. Later, when the growth rate reaches a saturation (see Figure 9a), there appears a nonzero % RO during $t = 160t_0$ to $t = 200t_0$. Note that we only regard the former interval of the nonzero % RO as a rolled-up stage. The change in total pressure in Figure 9c increases with time at the midplane (Y_{mid}, green solid line) and reaches its maximum at time $t = 88t_0$ (time snapshot in Figure 10a), at the highest value among other Y locations, and then decreases with time until around $t = 122t_0$. As expected, this change at Y locations away from the midplane is weaker. The maximum of ΔP on the magnetosheath side ($Y_{mid} + \lambda_{KH}/8$, yellow solid line) is lower than that on the magnetospheric side ($Y_{mid} - \lambda_{KH}/8$, blue solid line). ΔP does not change much during the saturation phase at around $t = 122t_0$ to $t = 200t_0$.

Figure 9d shows that the change in magnetic curvature radius decreases with time. This is due to the development of the roll-up at midplane (green solid line). Despite the fluctuation, it can be seen that the change ΔR_c reaches its first local minimum at value $\sim 10\lambda_{KH}$ approximately when ΔP reaches its maximum. During $t = 88t_0 - 122t_0$, the trend of ΔR_c at midplane increases from $10\lambda_{KH}$ to $100\lambda_{KH}$, in contrast to the magnetosheath side where it decreases from $100\lambda_{KH}$ to $10\lambda_{KH}$. ΔR_c at all Y locations stays low at value $\sim 10\ \lambda_{KH}$ after $t = 122t_0$. Overall, ΔR_c fluctuates more on the magnetospheric side, showing more activity of bending of magnetic field compared to at the magnetopause and on the magnetosheath side.

Figure 9e shows that the changes in vorticity ($\Delta\Omega_z$) at midplane and on the magnetospheric side increase with time until around $t = 80t_0$. Then they approximately reach a plateau with a value $\sim 0.5t_0^{-1}$ until around $t = 120t_0$ at these locations. To justify this vorticity saturation, we suggest an explanation as follows. The change $\Delta\Omega_z = \Omega_{z,max} - \Omega_{z,min}$ along the midplane increases with time as the wave amplitude grows because it is more perturbed from sinusoids. Once the wave amplitude has significantly grown, the virtual probes should detect $\Omega_{z,min} = 0$ at nonshear layer regions; therefore, $\Delta\Omega_z \approx \Omega_{z,max}$. This $\Omega_{z,max}$ is limited by the scaling value $\Omega_z \sim (V_2 - V_1)/a = 0.5t_0^{-1}$, given that there is no further rolling within the vortex. However, $\Delta\Omega_z$ further increases after $t = 120t_0$ and reaches its global maximum with a value of $2(V_2 - V_1)/a$ around $t = 160t_0$. We will next

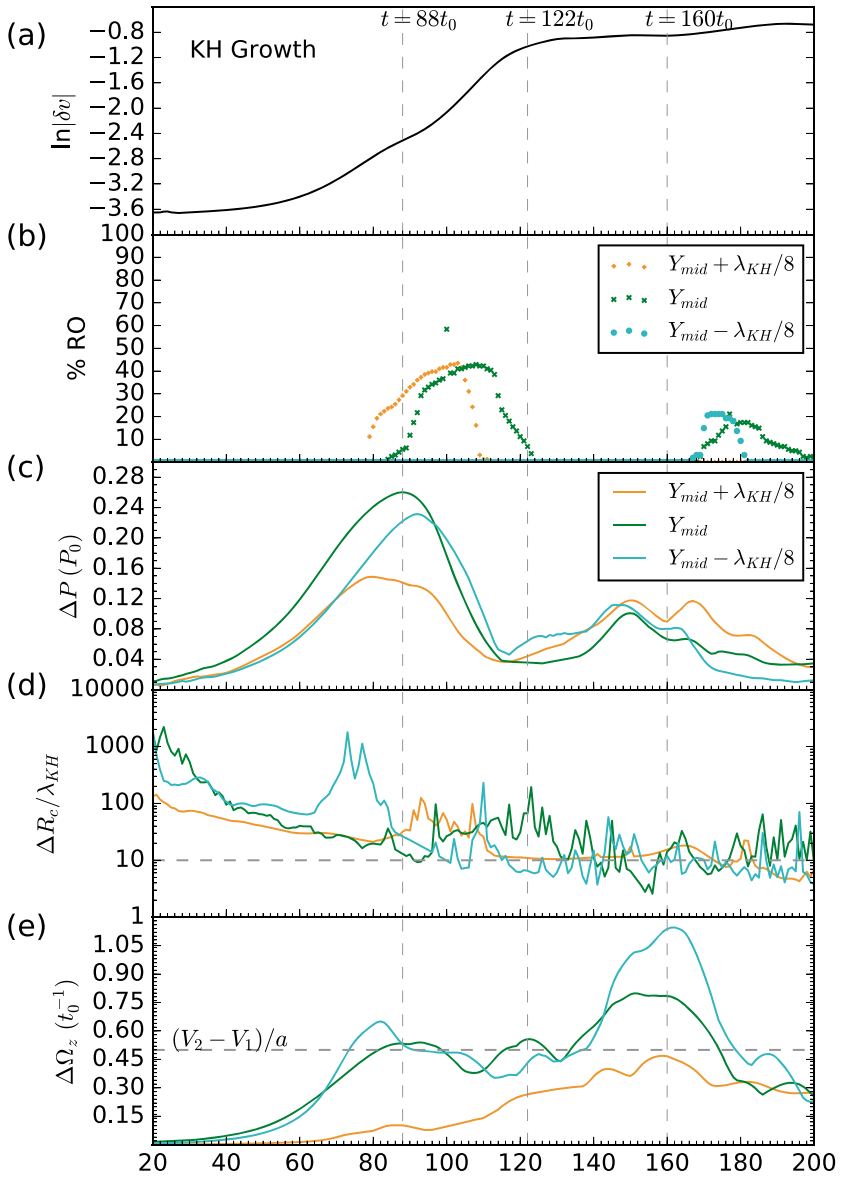

Figure 9. KH wave evolution. (a) Average velocity perturbation (KH growth), (b) percentage of roll-up (percentage of ions that satisfy LDFTS plasma criteria), (c) changes of total pressure, (d) curvature radius, and (e) vorticity as a function of time. The changes in Figures 9c–9e are calculated from the difference between the maximum and minimum values at a given *Y* location within *X* range of one wavelength.

investigate this high change of vorticity. On the magnetosheath side, $\Delta\Omega_z$ gradually increases until $t = 160t_0$, with much lower magnitude compared to other *Y* locations.

To understand the change in vorticity, we show time snapshots of vorticity at chosen times $t = 88t_0$, $122t_0$, and $160t_0$ in Figures 10a–10c, respectively (for full time sequence, see Movie S2 in the supporting information). The first maximum in $\Delta\Omega_z$ at $t = 88\ t_0$ (Figure 9e) is associated with the development of the rolled-up vortex in Figure 10a. The second peak of Ω_z at $t = 122t_0$ (Figure 9e) is associated with the development of the negative vorticity layer (blue in Figure 10b) in the rolled-up envelope on the magnetospheric side of the magnetopause, hereafter referred to a "turnover layer." This turnover layer persists after the KH growth reaches a saturation and becomes stronger in vorticity magnitude (blue in Figure 10c), giving rise to the global peak around $t = 160t_0$ (Figure 9e) with strongest value in the magnetospheric side. This negative vorticity layer is reminiscent of the rolled-up history on the duskside magnetopause (the positive vorticity layer is expected on the dawnside).

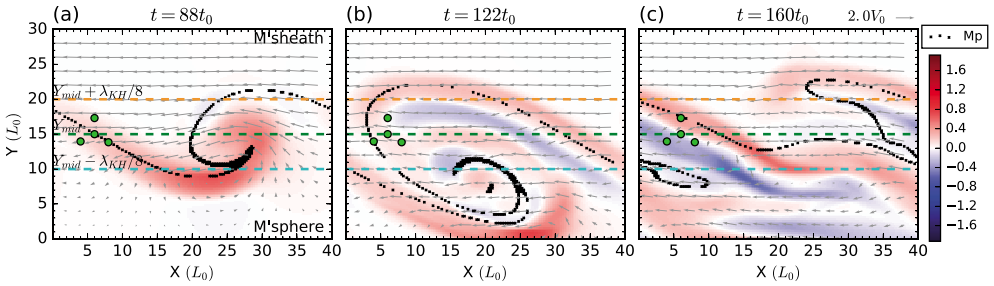

Figure 10. Evolution of flow vorticity in KH waves. This is the same format as Figure 7. (a) at $t = 88t_0$, (b) at $t = 122t_0$, and (c) at $t = 160t_0$. Gray vectors represent the velocity field in the static frame of magnetosphere. Green dots show static spacecraft positions (the same as Figure 1a). Dashed lines represent four-spacecraft barycenters and correspond to Figures 9b–9e. For an animation of this sequence, see Movie S2 in the supporting information.

5. Summary and Discussion

We have analyzed magnetic curvature and vorticity in Kelvin-Helmholtz instability in a 2.5-D MHD simulation using four-spacecraft techniques, using increasing (regular) tetrahedron sizes of virtual spacecraft. This is important to understand magnetic distortion and vortical flow induced by KH waves spatially and temporally for future analyses with real data. Our main results are as follows.

Magnetic curvature radius and direction vary depending on the sizes of the tetrahedron. This shows that there are no such "exact" values as they all depend on the structure we want to characterize (see Figure 4). For our particular example, this dependence is found to be linear in range of $a = [3L_0, 10L_0]$, ($[0.075\lambda_{KH}, 0.25\lambda_{KH}]$), especially at the leading and trailing edges of the nonlinear KH wave. This linear increase breaks when the tetrahedron size becomes larger than a quarter of the KH wavelength ($10L_0$). The magnetic curvature erratically varies in the smaller range $a = [L_0/4, 3L_0]$, ($[0.00625\lambda_{KH}, 0.075\lambda_{KH}]$), particularly in the vicinity of the vortex center. This illustrates how the KH vortex system may be understood on three scale ranges in which the linear and nonlinear structures of KH waves may be expected. This also suggests that for a comprehensive understanding of the KH phenomenon, a cross-scale coverage of KH observations would be needed, best represented by three nested scales of spacecraft tetrahedron. Using a multiscale tetrahedron size may also be useful for cross-scale KH studies, that is, as recently reported for cross-scale energy transport from fluid to ion scales inside a KH vortex (Moore et al., 2016).

MCA has revealed the detailed magnetic curvature of KH waves. Depending on tetrahedron size, specific regions are resolved. For the range of interspacecraft separations in our studies, $a = [L_0/4, 4L_0]$, ($[0.00625\lambda_{KH}$, $0.1\lambda_{KH}]$), we resolve the so-called KH "spine" reported by Otto and Fairfield (2000, and reference therein), marked by sharp gradient in B_z and different polarity of B_x and B_y. We report that this KH spine associated with the magnetospheric boundary layer is characterized by curvature opposite to the wave propagation direction. We further report the existence of a magnetosheath boundary layer characterized by curvature in the wave propagation direction. Magnetic curvature against the shear flow in the magnetospheric boundary layer may be a consequence from plasma motion, which drags along the magnetic field into the rotating vortex. Twisting of magnetic field lines around the vortex can be clearly seen from a gradual change of curvature direction both on the magnetosheath and magnetospheric sides. However, our simulation suggests that this twisting pattern can only be resolved on the magnetosheath side (so-called "magnetosheath vortex") for every tested tetrahedron size. Identifying these vortex regions in spacecraft data using curvature would be useful for sketching the magnetic geometry around a spacecraft trajectory, which can complement studies of other KH wave-induced mechanisms such as magnetic reconnection.

A train of rotating vortices would give rise to periodical vorticity peaks, and these may be indicative of rolled-up KH vortices. This is illustrated in spatial studies (section 4.1) in which we have shown the clear enhanced vorticity interval during the vortex center passage. In temporal studies (section 4.2) there are similar pulses but not all of them correspond to vortex centers, identified by minimum total pressure (i.e., at $t = 138t_0$ and $162t_0$). At these times the total pressure shows neither a minimum nor a maximum, but the magnetic field data show characteristics of KH spines (consistent with magnetic curvature direction and curvature radius). The vorticity peaks at these times arise from the shear flow layer. This can be observed by negative vorticity dips before positive peaks, showing passages of a turnover layer, which is sandwiched between the vortex

center and the KH spine. We explain this negative vorticity layer as a result of the rolling-up process in which the vortex core has a stronger (positive) vorticity than the outer vortex regions near the magnetopause (original shear layer): the sandwiched, more tenuous magnetospheric plasma, which has zero vorticity initially, is susceptible to a reversed flow direction. This effect is clearly seen in Figures 1, 7, and 8 and Movie S2. The negative vorticity may also correspond to the "reversed shear flow" described by Nakamura et al. (2004) in two-fluid simulations (there, this phenomenon was found to be related to the presence of a density jump as expected in our case at the magnetopause). In addition, we would like to point out that these shear layer crossings can give rise to periodic pulse-enhanced vorticity, even though the probes are not crossing through vortex centers. The pulse-enhanced vorticity Ω_z, together with current density J_z, is also found when spacecraft transit from magnetopause to magnetosheath in three-spacecraft studies of KH waves by Shen et al. (2012). However, to pinpoint if spacecraft are passing the vortex center of a rolled-up vortex, a strong vorticity peak due to the rotating vortex in between two smaller peaks of vorticity from KH spines should be visible. Vorticity time series in Figure 8 during the transits (2) and (3) show a perfect example of a rolled-up vortex passage.

Change in curvature radius and vorticity with time may be indicative of different stages of KH wave development. The significant decrease of $\Delta R_c(t)$, from 1,000 to 10 λ_{KH}, in the transition from linear to nonlinear stage implies structural evolution in the magnetic field (consistent with Ryu et al., 2000), especially on the magnetospheric side. The flow vorticity $\Delta\Omega_z(t)$ saturates at the expected scaling value $\Delta V/a$, where ΔV would be limited by the spacecraft separation, for fully rolled-up vortices. We suggest that observed $\Delta\Omega_z$ larger than the scaling value correspond to the development of a turnover layer, which possesses negative vorticity (for duskside magnetopause). This layer exists in an elongated vortex, on the magnetospheric side of the magnetopause, in which a relative clockwise flow rotation can locally develop. Since this layer persists after the KH growth has saturated, it may be used as an indicator for a roll-up history of KH waves.

This work illustrates an example of combined four-spacecraft methods, with important applications to consider for analysis and interpretation of real spacecraft data. There are various limitations or simplifications to keep in mind. For instance, our results on magnetic curvature depended on the initial magnetic field configuration: finite curvature in the simulation is a consequence of an initial B_x component; in the absence of B_x, magnetic curvature would be zero everywhere. Asymmetric magnetic field B_z on both sides of magnetopause could result in more complex signatures (e.g., Nakamura & Daughton, 2014) and should be taken into account when interpreting real data. Also, nonalignment of B_z at the magnetopause surface, for example, when IMF clock angle is nonzero, may already create a region of small curvature radius at the transition layers. Adding complexity to the model setup will not affect the qualitative results at the magnetopause, namely, (1) the dependence of magnetic curvature on the tetrahedron sizes, (2) the detailed magnetic curvature characterization, and (3) the vorticity signatures of the KH waves (i.e., spatial variations across a KH wavelength and temporal nonlinear development). It may be useful to note that some of the vorticity signatures may occur because of the specificities of the magnetopause environment such as the presence of a density jump. In particular, previous studies indicate a shift between the centers of velocity and density profiles, which change the conditions for vortex formation (Rossi, 2015). The observed signatures in our simulations will be shifted toward the vicinity of a KH vortex in cases where the shear layer is located away from the magnetopause (not shown). Nonideal configurations of the spacecraft tetrahedron would affect gradient estimations and, subsequently, the quality of the MCA estimates. In addition, our 2.5-D results are applicable mainly in the equatorial plane. Finally, the chosen KH wavelength does not impact on the qualitative results listed above as it only represents the physical scale of the KH structure with respect to the tetrahedron scale. Future works include an extension of our results to consider the applications in the higher latitudes by applying the techniques in 3-D simulations. Finally, we aim to apply both four-spacecraft techniques in future work with the availability of in situ data from two different four-spacecraft missions Cluster and MMS.

Acknowledgments
R. K. acknowledges financial support from CEMPS at the University of Exeter. C. F. acknowledges financial support from the UK Science and Technology Facilities Council (STFC) under her Advanced Fellowship ST/I003649. Simulation data used in this study were generated using the Lare2D code (open-access at https://ccpforge.cse.rl.ac.uk/gf/project/lare2d/) with thanks to Tony Arber's team at the University of Warwick.

References

Arber, T. D., Longbottom, A. W., Gerrard, C. L., & Milne, A. M. (2001). A staggered grid, Lagrangian-Eulerian Remap code for 3-D MHD simulations. *Journal of Computational Physics*, *171*, 15–181. https://doi.org/10.1006/jcph.2001.6780

Bavassano Cattaneo, M. B., Marcucci, M. F., Bogdanova, Y. V., Réme, H., Dandouras, I., Kistler, L. M., & Lucek, E. (2010). Global reconnection topology as inferred from plasma observations inside Kelvin-Helmholtz vortices. *Annales Geophysicae*, *28*(4), 893–906. https://doi.org/10.5194/angeo-28-893-2010

Burch, J. L., Moore, T. E., Torbert, R. B., & Giles, B. L. (2015). Magnetospheric Multiscale overview and science objectives. *Space Science Reviews*, *199*, 5–21. https://doi.org/10.1007/s11214-015-0164-9

Cao, D., Fu, H. S., Cao, J. B., Wang, T. Y., Graham, D. B., Chen, Z. Z., … Burch, J. L. (2017). MMS observations of whistler waves in electron diffusion region. *Geophysical Research Letters*, *44*, 3954–3962. https://doi.org/10.1002/2017GL072703

Chanteur, G. (1998). Spatial interpolation for four spacecraft: Theory. In G. Paschmann & P. W. Daly (Eds.), *Analysis methods for multi-spacecraft data* (chap. 14, pp. 349–370). Bern: ISSI Scientific Report SR-001.

Collado-Vega, Y. M., Kessel, R. L., Sibeck, D. G., Kalb, V. L., Boller, R. A., & Rastaetter, L. (2013). Comparison between vortices created and evolving during fixed and dynamic solar wind conditions. *Annales Geophysicae*, *31*, 1463–1483. https://doi.org/10.5194/angeo-31-1463-2013

Consolini, G., Materassi, M., Marcucci, M. F., & Pallocchia, G. (2015). Statistics of the velocity gradient tensor in space plasma turbulent flows. *Astrophysical Journal*, *812*(1), 84. https://doi.org/10.1088/0004-637X/812/1/84

De Keyser, J., & Roth, M. (2003). Structural analysis of periodic surface waves on the magnetospheric boundary. *Planetary and Space Science*, *51*(12), 757–768. https://doi.org/10.1016/S0032-0633(03)00112-0

Dunlop, M. W., Southwood, D. J., Glassmeier, K. H., & Neubauer, F. M. (1988). Analysis of multipoint magnetometer data. *Advances in Space Research*, *8*, 273–277. https://doi.org/10.1016/0273-1177(88) 90141-X

Escoubet, C. P., Fehringer, M., & Goldstein, M. (2001). The Cluster mission. *Annales Geophysicae*, *19*, 1197–1200. https://doi.org/10.5194/angeo-19-1197-2001

Faganello, M., Califano, F., Pegoraro, F., & Andreussi, T. (2012). Double mid-latitude dynamical reconnection at the magnetopause: An efficient mechanism allowing solar wind to enter the Earth's magnetosphere. *Europhysics Letters*, *100*(6), 69001. https://doi.org/10.1209/0295-5075/100/69001

Foullon, C., Farrugia, C. J., Fazakerley, A. N., Owen, C. J., Gratton, F. T., & Torbert, R. B. (2008). Evolution of Kelvin-Helmholtz activity on the dusk flank magnetopause. *Journal of Geophysical Research*, *113*, A11203. https://doi.org/10.1029/2008JA013175

Fu, H. S., Vaivads, A., Khotyaintsev, Y. V., Olshevsky, V., André, M., Cao, J. B., … Lapenta, G. (2015). How to find magnetic nulls and reconstruct field topology with MMS data? *Journal of Geophysical Research: Space Physics*, *120*, 3758–3782. https://doi.org/10.1002/2015JA021082

Gurgiolo, C., Goldstein, M. L., Viñas, A.-F., & Fazakerley, A. N. (2010). First measurements of electron vorticity in the foreshock and solar wind. *Annales Geophysicae*, *28*, 2187–2200. https://doi.org/10.5194/angeo-28-2187-2010

Harvey, C. C. (1998). Spatial gradients and the volumetric tensor. In G. Paschmann & P. W. Daly (Eds.), *Analysis methods for multi-spacecraft data* (chap. 12, pp. 307–322). Bern: ISSI Scientific Report SR-001.

Hasegawa, H., Fujimoto, M., Takagi, K., Saito, Y., Mukai, T., & Réme, H. (2006). Single-spacecraft detection of rolled-up Kelvin-Helmholtz vortices at the flank magnetopause. *Journal of Geophysical Research*, *111*, A09203. https://doi.org/10.1029/2006JA011728

Hasegawa, H., Sonnerup, B. U. Ö., Fujimoto, M., Saito, Y., & Mukai, T. (2007). Recovery of streamlines in the flank low-latitude boundary layer. *Journal of Geophysical Research*, *112*, A04213. https://doi.org/10.1029/2006JA012101

Hasegawa, H., Retinó, A., Vaivads, A., Khotyaintsev, Y., André, M., Nakamura, T. K. M., … Canu, P. (2009). Kelvin-Helmholtz waves at the Earth's magnetopause: Multiscale development and associated reconnection. *Journal of Geophysical Research*, *114*, A12207. https://doi.org/10.1029/2009JA014042

Horton, W., Perez, J. C., Carter, T., & Bengtson, R. (2005). Vorticity probes and the characterization of vortices in the Kelvin-Helmholtz instability in the large plasma device experiment. *Physics of Plasmas*, *12*(2), 22,303–22,308. https://doi.org/10.1063/1.1830489

Lavraud, B., Zhang, Y. C., Vernisse, Y., Gershman, D. J., Dorelli, J., Cassak, P. A., … Yokota, S. (2016). Currents and associated electron scattering and bouncing near the diffusion region at Earth's magnetopause. *Geophysical Research Letters*, *43*, 3042–3050. https://doi.org/10.1002/2016GL068359

Leroy, M. H. J., & Keppens, R. (2017). On the influence of environmental parameters on mixing and reconnection caused by the Kelvin-Helmholtz instability at the magnetopause. *Physics of Plasmas*, *24*, 12906. https://doi.org/10.1063/1.4974758

Lin, D., Wang, C., Li, W., Tang, B., Guo, X., & Peng, Z. (2014). Properties of Kelvin-Helmholtz waves at the magnetopause under northward interplanetary magnetic field: Statistical study. *Journal of Geophysical Research*, *119*, 7485–7494. https://doi.org/10.1002/2014JA020379

Miura, A. (1984). Anomalous transport by magnetohydrodynamic Kelvin-Helmholtz instabilities in the solar wind-magnetosphere interaction. *Journal of Geophysical Research*, *89*(A2), 801–812. https://doi.org/10.1029/JA089iA02p00801

Miura, A. (1987). Kelvin-Helmholtz instability at the magnetospheric boundary. *Geophysical Research Letters*, *12*(10), 635–638. https://doi.org/10.1029/GL012i010p00635

Matsumoto, Y., & Hoshino, M. (2004). Onset of turbulence induced by a Kelvin-Helmholtz vortex. *Geophysical Research Letters*, *31*, L02807. https://doi.org/10.1029/2003GL018195

Moore, T. W., Nykyri, K., & Dimmock, A. P. (2016). Cross-scale energy transport in space plasmas. *Nature Physics*, *12*, 1164–1169. https://doi.org/10.1038/NPHYS3869

Nakamura, T. K. M., Hayashi, D., Fujimoto, M., & Shinohara, I. (2004). Decay of MHD-scale Kelvin-Helmholtz vortices mediated by parasitic electron dynamics. *Physical Review Letters*, *92*(14), 145001. https://doi.org/10.1103/PhysRevLett.92.145001

Nakamura, T. K. M., Daughton, W., Karimabadi, H., & Eriksson, S. (2013). Three-dimensional dynamics of vortex-induced reconnection and comparison with THEMIS observations. *Journal of Geophysical Research: Space Physics*, *118*, 5742–5757. https://doi.org/10.1002/jgra.50547

Nakamura, T. K. M., & Daughton, W. (2014). Turbulent plasma transport across the Earth's low-latitude boundary layer. *Geophysical Research Letters*, *41*, 8704–8712. https://doi.org/10.1002/2014GL061952

Nishino, M. N., Fujimoto, M., Ueno, G., Mukai, T., & Saito, Y. (2007). Origin of temperature anisotropies in the cold plasma sheet: Geotail observations around the Kelvin-Helmholtz vortices. *Annales Geophysicae*, *25*, 2069–2086. https://doi.org/10.5194/angeo-25-2069-2007

Nykyri, K., & Otto, A. (2001). Plasma transport at the magnetospheric boundary due to reconnection in Kelvin-Helmholtz vortices. *Geophysical Research Letters*, *28*, 3565–3568. https://doi.org/10.1029/2001GL013239

Otto, A., & Fairfield, D. H. (2000). Kelvin-Helmholtz instability at the magnetotail boundary: MHD simulation and comparison with Geotail observations. *Journal of Geophysical Research*, *105*(A9), 21,175–21,190. https://doi.org/10.1029/1999JA000312

Owen, C. J., Taylor, M. G. G. T., Krauklis, I. C., Fazakerley, A. N., Dunlop, M. W., & Bosqued, J. M. (2004). Cluster observations of surface waves on the dawn flank magnetopause. *Annales Geophysicae*, *22*(3), 971–983. https://doi.org/10.5194/angeo-22-971-2004

Parashar, T. N., & Matthaeus, W. H. (2016). Propinquity of current and vortex structures: Effects on collisionless plasma heating. *Astrophysical Journal*, *832*(1), 57. https://doi.org/10.3847/0004-637X/832/1/57

Phan, T. D., Eastwood, J. P., Cassak, P. A., Øieroset, M., Gosling, J. T., Gershman, D. J., … Wilder, F. D. (2016). MMS observations of electron-scale filamentary currents in the reconnection exhaust and near the X line. *Geophysical Research Letters*, *43*, 6060–6069. https://doi.org/10.1002/2016GL069212

Plaschke, F., Taylor, M. G. G. T., & Nakamura, R. (2014). Alternative interpretation of results from Kelvin-Helmholtz. *Geophysical Research Letters*, *41*, 244–250. https://doi.org/10.1002/2013GL058948

Plaschke, F., Kahr, N., Fischer, D., Nakamura, R., Baumjohann, W., Magnes, W., … Kepko, E. L. (2016). Steepening of waves at the duskside magnetopause. *Geophysical Research Letters*, *43*, 7373–7380. https://doi.org/10.1002/2016GL070003

Robert, P., Roux, A., Harvey, C. C., Dunlop, M. W., Daly, P. W., & Glassmeier, K. H. (1998). Tetrahedron geometric factors. In G. Paschmann & P. W. Daly (Eds.), *Analysis methods for multi-spacecraft data* (chap. 13, pp. 323–328). Bern: ISSI Scientific Report SR-001.

Robert, P., Dunlop, M. W., Roux, A., & Chanteur, G. (1998). Accuracy of current density determination. In G. Paschmann & P. W. Daly (Eds.), *Analysis methods for multi-spacecraft data* (chap. 16, pp. 395–418). Bern: ISSI Scientific Report SR-001.

Rossi, C. (2015). Kelvin-Helmholtz instability at the magnetopause: Theory and observations. Astrophysics [astro-ph]. Université Pierre et Marie Curie - Paris VI, NNT: 2015PA066140. Retrieved from https://tel.archives-ouvertes.fr/tel-01222912

Runov, A., Nakamura, R., & Baumjohann, W. (2006). Multi-point study of the magnetotail current sheet. *Advances in Space Research*, *38*(1), 85–92. https://doi.org/10.1016/j.asr.2004.09.024

Russell, C. T., Gosling, J. T., Zwickl, R. D., & Smith, E. J. (1983). Multiple spacecraft observations of interplanetary shocks: ISEE three-dimensional plasma measurements. *Journal of Geophysical Research*, *88*(A12), 9941–9947. https://doi.org/10.1029/JA088iA12p09941

Ryu, D., Jones, T. W., & Frank, A. (2000). The magnetohydrodynamic Kelvin-Helmholtz instability: A three-dimensional study of nonlinear evolution. *Astrophysical Journal*, *545*, 475–493. https://doi.org/10.1086/317789

Sahraoui, F., Belmont, G., Goldstein, M. L., & Rezeau, L. (2010). Limitations of multispacecraft data techniques in measuring wave number spectra of space plasma turbulence. *Journal of Geophysical Research*, *115*, A04206. https://doi.org/10.1029/2009JA014724

Sonnerup, B. U. Ö., Hasegawa, H., Teh, W.-L., & Hau, L.-N. (2006). Grad-Shafranov reconstruction: An overview. *Journal of Geophysical Research*, *111*, A09204. https://doi.org/10.1029/2006JA011717

Shen, C., Li, X., Dunlop, M., Liu, Z. X., Balogh, A., Baker, D. N., … Wang, X. (2003). Analyses on the geometrical structure of magnetic field in the current sheet based on Cluster measurements. *Journal of Geophysical Research*, *108*, 1168. https://doi.org/10.1029/2002JA009612

Shen, C., Liu, Z. X., Li, X., Dunlop, M., Lucek, E., Rong, Z. J., … Mouikis, C. (2008). Flattened current sheet and its evolution in substorms. *Journal of Geophysical Research*, *113*, A07S21. https://doi.org/10.1029/2007JA012812

Shen, C., Rong, Z. J., Dunlop, M. W., Ma, Y. H., Li, X., & Zeng, G. (2012). Spatial gradients from irregular, multiple-point spacecraft configurations. *Journal of Geophysical Research*, *117*, A11207. https://doi.org/10.1029/2012JA018075

Shen, C., Yang, Y. Y., Rong, Z. J., Li, X., Dunlop, M., Carr, C. M., … Zeng, G. (2014). Direct calculation of the ring current distribution and magnetic structure seen by Cluster during geomagnetic storms. *Journal of Geophysical Research: Space Physics*, *119*, 2458–2465. https://doi.org/10.1002/2013JA019460

Takagi, K., Hashimoto, C., Hasegawa, H., Fujimoto, M., & TanDokoro, R. (2006). Kelvin-Helmholtz instability in a magnetotail flank-like geometry: Three-dimensional MHD simulations. *Journal of Geophysical Research*, *111*, A08202. https://doi.org/10.1029/2006JA011631

Taylor, M. G. G. T., & Lavraud, B. (2008). Observation of three distinct ion populations at the Kelvin-Helmholtz-unstable magnetopause. *Annales Geophysicae*, *26*, 1559–1566. https://doi.org/10.5194/angeo-26-1559-2008

Taylor, M. G. G. T., Hasegawa, H., Lavraud, B., Phan, T., Escoubet, C. P., Dunlop, M. W., … Wild, J. A. (2012). Spatial distribution of rolled up Kelvin-Helmholtz vortices at Earth's dayside and flank magnetopause. *Annales Geophysicae*, *30*, 1025–1035. https://doi.org/10.5194/angeo-30-1025-2012

Vernisse, Y., Lavraud, B., Eriksson, S., Gershman, D. J., Dorelli, J., Pollock, C., … Yokota, S. (2016). Signatures of complex magnetic topologies from multiple reconnection sites induced by Kelvin-Helmholtz instability. *Journal of Geophysical Research: Space Physics*, *121*, 9926–9939. https://doi.org/10.1002/2016JA023051

Vogt, J., & Paschmann, G. (1998). Accuracy of plasma moment derivatives. In G. Paschmann & P. W. Daly (Eds.), *Analysis methods for multi-spacecraft data* (chap. 17, pp. 419–447). Bern: ISSI Scientific Report SR-001.

Wu, C. C. (1986). Kelvin-Helmholtz instability at the magnetopause boundary. *Journal of Geophysical Research*, *91*(A3), 3042–3060. https://doi.org/10.1029/JA091iA03p03042

Yang, Y. Y., Shen, C., Zhang, Y. C., Rong, Z. J., Li, X., & Dunlop, M. (2014). The force-free configuration of flux ropes in geomagnetotail: Cluster observations. *Journal of Geophysical Research: Space Physics*, *119*, 6327–6341. https://doi.org/10.1002/2013JA019642

Zhang, Y. C., Shen, C., Liu, Z. X., Rong, Z. J., Zhang, T. L., Marchaudon, A., … Dandouras, I. (2013). Two different types of plasmoids in the plasma sheet: Cluster multisatellite analysis application. *Journal of Geophysical Research: Space Physics*, *118*, 5437–5444. https://doi.org/10.1002/jgra.50542

Zhang, Y. C., Shen, C., Marchaudon, A., Rong, Z. J., Lavraud, B., Fazakerley, A., … Liu, Z. X. (2016). First in situ evidence of electron pitch angle scattering due to magnetic field line curvature in the Ion diffusion region. *Journal of Geophysical Research: Space Physics*, *121*, 4103–4110. https://doi.org/10.1002/2016JA022409